Visualization and Reduction of Mutual Coupling Between Antennas Installed on a Platform

Johan Lundgren, Johan Malmström, Jari-Matti Hannula, and B. L. G. Jonsson

***Abstract*—Mutual coupling, or equivalently, the isolation between antennas, is a key parameter in antenna system design. In this work, a new quantity is proposed to obtain spatial information about mutual coupling. The new quantity is named the weak-coupling density. This quantity is a real-valued scalar and can be visualized as a three-dimensional density in space. It is also shown that there is a strong correlation between regions with a positive (negative) weak-coupling density and decreasing (increasing) the coupling when placing an absorber in that region. This predictive ability is a useful feature, which is tested here for three numerical cases. The results are robust to the shape of the platform, and it persists over neighboring frequencies. By placing absorbers based on the weak-coupling density, it is possible to reduce the required amount of absorbers to obtain a certain mutual coupling reduction. The visualization results and predictions of absorber positions are compared with a Poynting vector based method. Placing absorbers based on the weak-coupling density had a larger impact on the mutual coupling, compared to the predictions with the Poynting vector based method in the investigated cases.**

***Index Terms*—Mutual coupling, isolation, visualization, reciprocity, reaction theorem**

I. Introduction

LOW isolation between antennas on a vehicle can degrade the overall system performance, since transmitted power of one antenna may leak into a receiving antenna of another system. This makes mutual coupling between antennas one of the key parameters for antenna system performance [1], in particular for antennas on vehicles where the distance between antennas is strongly constrained. Methods to reduce mutual coupling between antennas date back to early antenna constructions [2]. A few recent publications on the subject include [3], [4] that utilized parasitic elements and [5]–[7], where electromagnetic bandgap structures [8] have been used. In [7], the possibility of using ferrite absorbers is also studied.

For complex vehicle platforms such as airplanes and ships, the mutual coupling consists of several contributions such as line-of-sight, edge-diffraction, creeping waves, and reflection coupling [1], [9], which complicates the process of placing absorbers to mitigate the mutual coupling. Visualization methods are therefore useful tools for identifying regions in space with strong contributions to the mutual coupling. A path between a transmitting and receiving antenna that depicts the spatial contribution to the mutual coupling is referred to as a coupling path [10], [11].

In this paper, based on the master's thesis in [12], a predictive visualization method of weak mutual coupling is proposed and numerically validated. The method uses reciprocity and it is based on the reaction theorem [13], [14]. The quantity proposed here is referred to as the *weak-coupling density* and has similarities with the impedance density defined in [10]. However, the weak-coupling density is real-valued and it is valid for non-ideal sources, which simplifies the calculation and makes the interpretation of the results straightforward. The ability of the weak-coupling density to predict regions in space with strong contributions the mutual coupling is numerically examined in three cases of increasing complexity.

Several other methods to visualize mutual coupling have been suggested in literature, including ray-tracing and diffuse scattering [15], [16]. These methods are generally not applicable to antennas installed on platforms since the near-field contribution can substantially contribute to the coupling.

A Poynting vector based method was defined in [17], [18] and applied [19], [20] to mitigate electromagnetic interference. The coupling paths are visualized by computing streamlines through the power flow between the receiving and transmitting antenna. The Poynting vector based method, in its current form, does not distinguish between incident and accepted power. Also, as seen in [20], the streamlines follow different paths depending on which antenna that is transmitting and receiving, even though the setup is reciprocal, see [21].

The method proposed here is a generalization of [10], [11], both of which are also based on the reciprocity theorem. One of the important extensions in this work is that the proposed method automatically handles arbitrary complex-valued self-impedances for the antennas, as well as both well and poorly matched impedances. Both are of particular interest when investigating out-of-band coupling, where the receiving antenna often is badly tuned [1]. The work in [11] mainly focuses on identifying coupling paths, whereas the work presented in this paper focuses on both identifying and affecting the coupling.

The weak-coupling density proposed here is shown to have the ability to predict good absorber placements for the reduction of the mutual coupling. This predictability is compared with the ability of the method based on the Poynting vector [17], [18]. The comparisons are shown through numerical simulations in CST Microwave Studio for different setups.

Manuscript received ?? ??, 2020; revised ?? ??, 2020. The work of J. Lundgren and J. Malmström has been supported by Saab Surveillance. The work of J.-M. Hannula has been supported by the Walter Ahlström Foundation. The work of B. L. G. Jonsson has been funded in part by VINNOVA within the competence center ChaseOn under the project iAA.

J. Lundgren is with the Division of Electromagnetic Engineering, KTH Royal Institute of Technology, 100 44 Stockholm, Sweden, and also with Saab Surveillance, 107 24 Stockholm, Sweden (e-mail: jlu8@kth.se).

J. Malmström is with the Saab Surveillance, 107 24 Stockholm, Sweden.

J.-M. Hannula and B. L. G. Jonsson are with the Division of Electromagnetic Engineering, KTH Royal Institute of Technology, 100 44 Stockholm, Sweden.

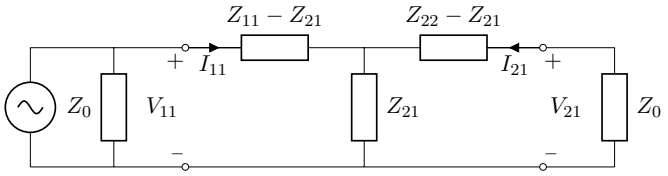

Fig. 1. A reciprocal two-antenna system seen as a two-port. The antennas and their mutual coupling are characterized by Z_{ij}, $i, j = 1, 2$. The antenna 1 is connected to a non-ideal current source with impedance Z_0 at Port 1 and a reference load Z_0 is connected to Port 2.

This paper is organized as follows. In Section II, the weak-coupling density is defined together with its properties and relation to mutual coupling. The methodology to compute and visualize the weak-coupling density between two antennas is described. The Poynting vector based method for visualization that is used as a reference is also described briefly in this section. In Section III, the possibility to use the weak-coupling density to predict absorber placement that reduces the mutual coupling is investigated. This is done through numerical simulations in CST Microwave Studio and by post-processing of the simulation data in Matlab for three different cases. The predictability of the weak-coupling density is compared to the Poynting vector based method. Finally, our conclusions are presented in Section IV.

II. Theory

A. Mutual Coupling

Mutual coupling between two antenna ports is defined as the received power in one port, normalized with the transmitted power in the other port, and is represented by the scattering parameter S_{21} [22]. The *isolation* between two antennas is defined as $1/|S_{21}|$. Another way to describe a two-port network is by impedance parameters, as shown in Fig. 1 for a reciprocal two-port. Expanding the relation between scattering and impedance parameters [22] in a Taylor series, in the limit of small Z_{21}, Z_{12} gives the first-order approximation

$$S_{21} \approx Z_{21} \frac{2Z_0}{(Z_{11} + Z_0)(Z_{22} + Z_0)}, \tag{1}$$

which is valid when

$$|(Z_{11} + Z_0)(Z_{22} + Z_0)| \gg |Z_{21} Z_{12}|. \tag{2}$$

Here, Z_{11} and Z_{22} are the self-impedances of Antenna 1 and Antenna 2, Z_{12} and Z_{21} are the mutual impedances between the two antennas, and Z_0 is the reference impedance. The influence of each impedance parameter on a reciprocal two-port circuit is depicted in Fig. 1. For the case of antennas with typically $50\,\Omega$ as reference impedance and a small mutual coupling, this approximation is useful. For antennas on a platform, it is often desired that the mutual impedance is orders of magnitude below the reference impedance Z_0. It is seen from (1) that the mutual impedance Z_{21} is to leading order proportional to S_{21} and it is therefore of interest to study Z_{21} when solving problems with weak antenna coupling.

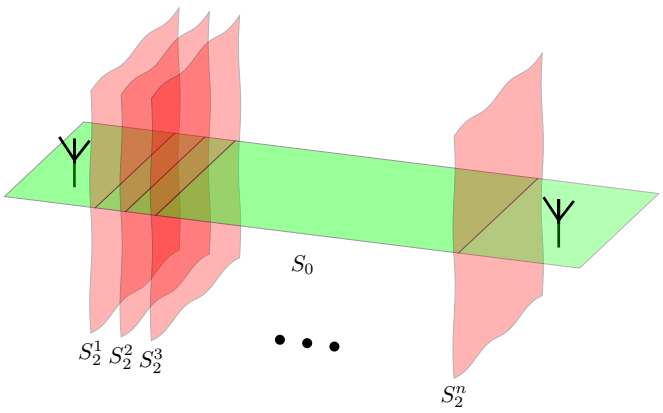

Fig. 2. Two antennas on a common platform with n red separation planes S_2 that construct a 3D representation of the coupling. The green plane S_0 illustrates a visualization plane.

B. Mutual Impedance and the Reaction Theorem

The reaction theorem [13], [14] offers a possibility to calculate the mutual impedance Z_{21} from the electric and magnetic fields $\boldsymbol{E}_1$ and $\boldsymbol{H}_1$, generated by exciting Antenna 1 with a current I_{11} according to the definition in Fig. 1. Subsequently, antenna 2 is excited with a current I_{22} by interchanging the position of the current source and the load Z_0 in Fig. 1, resulting in the fields $\boldsymbol{E}_2, \boldsymbol{H}_2$. The mutual impedance, Z_{21}, is then determined by

$$Z_{21} = \frac{V_{21}}{I_{11}} = \frac{\eta}{I_{11} I_{22}} \oint_{S_2} (\boldsymbol{E}_1 \times \boldsymbol{H}_2 - \boldsymbol{E}_2 \times \boldsymbol{H}_1) \cdot \hat{\boldsymbol{n}} \mathrm{d}S, \tag{3}$$

where S_2 is a surface that only encloses Antenna 2, and $\hat{\boldsymbol{n}}$ is an outward pointing normal to S_2. The factor η accounts for non-ideal current sources and a load connected to the receiving antenna [14] and is given by

$$\eta = \left(\frac{Z_{\text{in2}} + Z_0}{Z_{22} + Z_0} \right), \quad Z_{\text{in2}} = Z_{22} - \frac{Z_{21} Z_{21}}{Z_0 + Z_{11}}. \tag{4}$$

For the case when the receiving antenna is an open circuit, $\eta = 1$. For a recent derivation of the coefficient η in (4) see [12]. The derivation is based on Thevenin's theorem for the driving currents I_{11}, I_{22} as defined in Fig.1. It can be extended to the case with different reference impedances in the two ports [12].

Using the approach with the correction factor η in (4) simplifies the simulation to determine the required fields in (3). This follows from the fact that the excitation of the antennas now can be done sequentially with a desired non-ideal source and arbitrary load for the same antenna geometry in both cases.

C. Coupling Visualization Using the Reaction Theorem

To determine Z_{21} it suffices to calculate the integral in (3) over a surface S_2 that encloses Antenna 2 but not Antenna 1. Indeed, it suffices to consider a finite truncated plane between the antennas to obtain Z_{21} with a negligible loss of precision of the mutual impedance, see [23].

In this paper, a separation plane will be used as integration surface S_2 in (3), which is illustrated in Fig. 2, where any of the red planes can be the integration surface that separate the

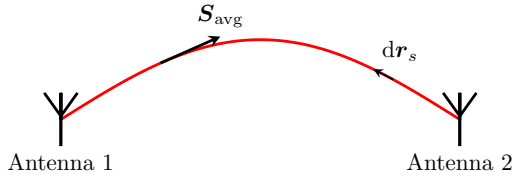

Fig. 3. The red line illustrates a streamline through the Poynting vector that visualize the coupling path between the antennas.

two antennas. Using any separation plane as the integration surface implies (3) that all the contributions to the mutual impedance exist on a single plane. An investigation of a sequence of separation planes S_2^m, $m = 1, \dots n$ as shown in Fig. 2 can hence provide information about the spatial distribution of the mutual coupling.

Multiplying both sides of (3) with the complex conjugate of Z_{21} gives a left-hand side equal to $|Z_{21}|^2$, which is real-valued and positive. The integral of the imaginary part in (3) must therefore be zero and the only contribution to $|Z_{21}|^2$ comes from the real part. Normalizing with $|Z_{21}|^2$ and omitting the imaginary part that will cancel out gives the following integrand in (3)

$$\delta = \mathrm{Re}\left\{\eta \frac{\boldsymbol{E}_1 \times \boldsymbol{H}_2 - \boldsymbol{E}_2 \times \boldsymbol{H}_1}{Z_{21} I_{11} I_{22}} \cdot \hat{\boldsymbol{n}}\right\}, \tag{5}$$

which is a real-valued, scalar, and time-invariant quantity with dimension $1/\mathrm{m}^2$ that varies with position. With the above definition of δ, equation (3) can be written as

$$1 = \oint_{S_2} \delta \, \mathrm{d}S. \tag{6}$$

The quantity δ studied in this work is approximately proportional to the normalized coupled power when the coupling is weak, as defined in (1) and (2). Therefore, δ is referred to as the *weak-coupling density*. A related approach was considered in [10] where the impedance density was defined.

The integration surface in (3) is arbitrary, as long as it separates the antennas. A 3D representation of the spatial variation of the mutual coupling contributions is constructed by calculating δ on several of the separation planes, from which it is possible to visualize the coupling on, e.g., the green plane S_0 in Fig. 2. It is important to remember that using the green horizontal plane S_0 as the integration surface in (3) will not give Z_{21}. However, it is useful for determining the distribution of how different regions in each vertical plane contribute to the mutual coupling and as visualization of this information.

D. The Poynting Vector

The above described method is compared with a method that is based on the time-averaged Poynting vector [17], [18]. In this type of visualization, streamlines are defined as being tangential to the vector field created by Poynting vectors. When Antenna 1 is radiating the power-flux goes from Antenna 1 to Antenna 2, and the streamline is thus the trace of the vector-field that connects back the power-flux that hit

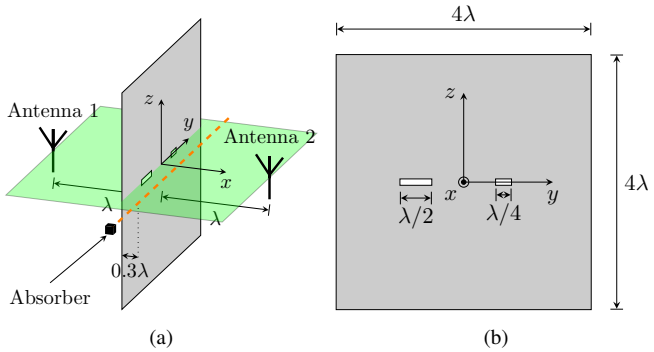

Fig. 4. A perforated screen that separates two dipole antennas. (a) The orange dashed line illustrates the path along which the black cube is swept. (b) Dimensions of the screen, where both slots have a height of $\lambda/10$.

Antenna 2 from Antenna 1. The path can be determined from the relations

$$\mathrm{d}\boldsymbol{r}_s \times \boldsymbol{S}_{\text{avg}} = 0, \quad \boldsymbol{S}_{\text{avg}} = \frac{1}{2}\mathrm{Re}\{\boldsymbol{E}_1 \times \boldsymbol{H}_1^*\} \tag{7}$$

starting from the location of the receiving antenna port. Fig. 3 shows the notation and illustrates a streamline from Antenna 2 when Antenna 1 transmits. The starting points of the streamlines are uniformly distributed on a cylindrical surface that is centered around and encloses the discrete port of the receiving antenna. This corresponds to the approach used by CST Microwave Studio.

III. Numerical Simulations

A. Perforated Screen

The first configuration on which the weak-coupling density is tested consists of two dipole antennas separated by a perfect electrical conductor (PEC) screen as shown in Fig. 4(a). The screen has two slots of dimension $\lambda/4$ and $\lambda/2$ respectively and height $\lambda/10$, as shown in Fig. 4(b). The slots are separated by the distance λ.

The widths and orientation of the slots were chosen such that the larger slot has a larger contribution to the mutual coupling than the smaller one. The frequency considered is 300 MHz. The dipoles are identical with length 448 mm, radius 3 mm, which gives the self-impedances $Z_{11} = Z_{22} = 65.7 - \mathrm{j}12.1\,\Omega$, the reference impedance is here set to $Z_0 = 50\,\Omega$. The mutual impedance $Z_{21} = 0.67 - \mathrm{j}0.92\,\Omega$, and the weak-coupling relation in (1) is satisfied.

This case is used for an initial comparison of the two visualization methods described in Section II. A question here is in which way one can compare the correctness of the predicted coupling paths or regions that contribute to a larger coupling. The approach to answer this question is to use a small absorber as a tool to determine the impact of a spatial region's local contribution to the mutual coupling. The absorber used here is a cube with side 0.1λ and material parameters $\varepsilon_r = 1 - \mathrm{j}2$, $\mu_r = 1 - \mathrm{j}2$. This electrically small absorber provides a perturbation of the initial setup to directly indicate the regional sensitivity on the mutual coupling.

The coupling is visualized in the green xy-plane seen in Fig. 4(a). Fig. 5(a) depicts the weak-coupling density, where

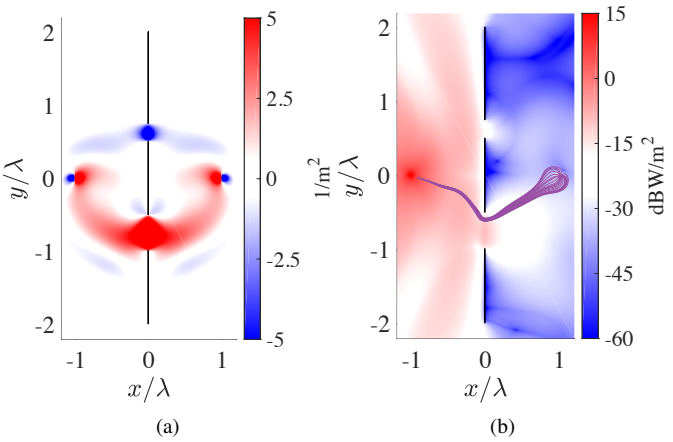

Fig. 5. Weak-coupling density and streamlines on the green plane in Fig. 4(a). (a) Weak-coupling density δ. (b) Magnitude of the Poynting vector $\boldsymbol{S}_{\text{avg}}$ in the background when Antenna 1 to the left transmits. The purple lines are 20 streamlines starting from the location of Antenna 2 to the right.

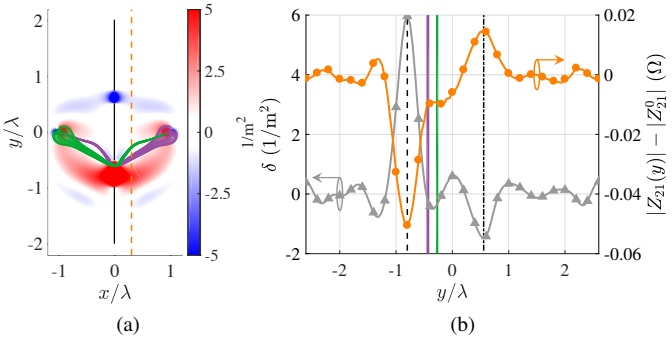

Fig. 6. Testing the predicted coupling contributions from the green plane in Fig. 4(a). (a) Weak-coupling density δ in the background and streamlines from $\boldsymbol{S}_{\text{avg}}$ in purple (green) when Antenna 1 (2) transmits. (b) The gray curve is δ along y at $x = 0.3\lambda$ in the green plane seen in Fig. 4(a). The orange curve is the impact on Z_{21} as a function of the y position of the cube. The purple and green vertical bars indicate where the streamlines pass.

the negative/positive weak-coupling density δ (blue/red density) is computed with (5), using $\hat{\boldsymbol{n}} = -\hat{\boldsymbol{x}}$. It is seen that δ has a positive (red) area that connects the the two antennas through the larger slot and a negative (blue) region that connects the antennas through the smaller slot. The magnitude of the Poynting vector $\boldsymbol{S}_{\text{avg}}$ computed with (7) is visualized in the background of Fig. 5(b). The purple lines connecting the two antennas through the larger slot in Fig. 5(b) are 20 streamlines computed with (7), when Antenna 1 on the left transmits. The starting points of the streamlines are uniformly distributed on a circle located in the green xy-plane depicted in Fig. 4(a). The circle has a radius of $\lambda/100$ and is centered at the port location of the receiving antenna.

In Fig. 6(a), the weak-coupling density is visualized in the background together with the purple streamlines from the Poynting vector when Antenna 1 transmits. Streamlines have also been computed when Antenna 2 on the right transmits, which are the 20 green lines in Fig. 6(a). It is seen that the streamlines starting from Antenna 1 do not follow the same path as the streamlines starting from Antenna 2, except at $x = 0$, as expected [21]. The red and blue areas of the weak-coupling density that connect the two antennas through the slots predict different regions with positive/negative contributions to the coupling, as compared with the Poynting vector based streamlines.

The gray curve with triangle marks in Fig. 6(b) shows the weak-coupling density, δ along the orange dashed line in Fig. 6(a), i.e., the contribution to the mutual coupling along the y-axis at $x = 0.3\lambda$. The vertical purple and green lines indicate the location where the streamlines in Fig. 6(a) pass $x = 0.3\lambda$ along the y-axis. Now, all the tools required to evaluate the accuracy of the predicted regions of strong coupling are in place. The mutual impedance Z_{21}^0 of the original problem is now perturbed by moving the above described absorber along the orange dashed line in Figs. 4(a) and 6(a).

The cube is placed at 105 points along the y-axis and the mutual impedance is simulated with CST Microwave Studio at each point. The orange curve with circles in Fig. 6(b) shows the impact of the cube on the mutual impedance as a function of the y-position. The depicted quantity is the mutual impedance deviation from the unperturbed case as a function of the y-position of the absorber $|Z_{21}(y)| - |Z_{21}^0|$.

The first thing to notice in Fig. 6(b) is the agreement between the weak-coupling density seen as the gray curve with triangles and the impact of the cube on the mutual impedance, shown with the orange curve with circles. The black dashed vertical line highlights the correlation between the positive peak of the weak-coupling density (indicating strong coupling) and the negative peak of the impact on the mutual impedance. Thus, an absorber in the region with the strongest weak-coupling density correlates well with the largest reduction of the mutual impedance. This means that by placing the cube in front of the larger slot, i.e., the red region in Fig. 6(a), the mutual impedance is decreased. Placing the cube where the intensity of δ is maximized will have the best effect on reducing the mutual impedance. Furthermore, it is seen that when the cube is located in the negative weak-coupling density as shown as a blue region in Fig. 6(a), i.e., the minimum of the gray curve with triangles in Fig. 6(b), the mutual impedance is increasing as highlighted with the black vertical dash-dotted line. By visualizing δ, it is possible to predict absorber locations that will either decrease or increase the mutual impedance.

Finally, it is seen that placing the cube on the Poynting vector streamlines, i.e., the purple and green vertical lines in Fig. 6(b), will only have a minor improvement impact on the mutual impedance in this configuration.

It has thus been demonstrated that it is possible to predict regions with strong coupling. The method used shows that it is possible to predict absorber locations that will decrease or increase the mutual impedance using δ. By visualizing δ on a plane that consists of several separation planes, as proposed in Section II, provides insight into how the coupling takes place between the antennas. With δ, it is seen from Fig. 6(a) that the contribution through the smaller slot partly cancels the coupling through the larger slot at the investigated frequency.

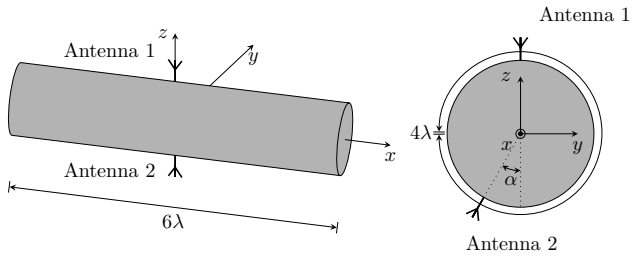

Fig. 7. A cylinder with two monopoles located in the yz-plane and equally far from the edges of the cylinder. Antenna 2 is rotated $\alpha = 11.25°$ from the bottom.

B. Cylinder model

To investigate how the presence of a platform impacts the coupling visualization, a PEC cylinder is used as a platform and two monopole antennas are mounted on it. One antenna on the top and one at the bottom as shown in Fig. 7. Perfectly matched layer (PML) boundary conditions were applied to the ends of the cylinder in the x-direction to reduce edge effects. The cylinder is 6λ long and has a 4λ circumference at 18 GHz. The two monopoles are identical with length 3.6 mm, and radius 0.05 mm. Both antennas are located equally far from the edges of the cylinder. Antenna 2 is rotated an angle $\alpha = 11.25°$ along the cylinder axis from the bottom to introduce a length difference between the power flowing on the left and right hand side of the cylinder. The self-impedance $Z_{11} = Z_{22} = 37.2 + \mathrm{j}1.5\,\Omega$ and the reference impedance $Z_0 = 50\,\Omega$ with a mutual impedance $Z_{21} = 0.35 - \mathrm{j}0.37\,\Omega$, which satisfy the weak-coupling requirement in (1).

The coupling is visualized with both the weak-coupling density and the Poynting vector based method. The case illustrated here is for the yz-plane that contains both the antennas, where Fig. 8(a) depicts the weak-coupling density δ computed with (5), using $\hat{\boldsymbol{n}} = \hat{\boldsymbol{z}}$. Fig. 8(b) depicts the magnitude of $\boldsymbol{S}_{\mathrm{avg}}$ in the background computed with (7) when Antenna 2 at the bottom transmits. The green lines in Fig. 8(b) are 40 streamlines computed with (7) that starts from the port location of Antenna 1 when Antenna 2 transmits. The starting points are uniformly distributed over two lines parallel to the port of Antenna 1, i.e. along the z-axis. The lines are located at a distance $\lambda/20$ from the port on the left- and right-hand side respectively.

It is seen in Fig. 8(a) that the right (left) hand side of the cylinder has a positive (negative) contribution. From the conclusions in Section III-A and the relation (1), it is therefore expected that placing an absorber on the left (right) hand side would increase (decrease) the mutual impedance and the mutual coupling. The streamlines of the Poynting vector are flowing on both sides of the cylinder as seen in Fig. 8(b). From the inset figure it is seen that 9 of the 40 streamlines are flowing on the left-hand side. Thus, the streamlines indicate that there is high coupling between the antennas on both sides of the cylinder, whereas the weak-coupling density indicates that only the right-hand side contributes to an increased coupling. To validate these two different predictions we add an absorber

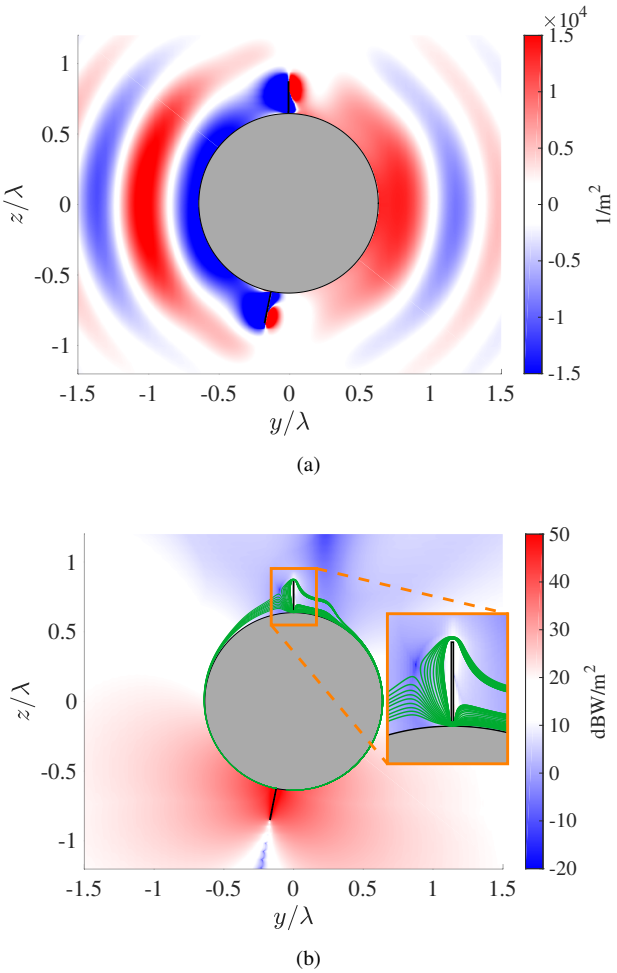

Fig. 8. Visualization results in the yz-plane that contains both the antennas, at 18 GHz. (a) Weak-coupling density δ. (b) Magnitude of $\boldsymbol{S}_{\mathrm{avg}}$ in the background with green streamlines when Antenna 2 transmits.

to the left- and right-hand side respectively, to one side of the cylinder at the time. Fig. 9(a) depicts the absorbers on the left- and right-hand side located equally far from the cylinder edges with length $L = \lambda$, width $w = 0.5\lambda$, and thickness $t = 1$ mm. The absorber used in this case is a Laird Q-Zorb 2338 surface wave absorbing material (SWAM) [24] that is intended for attenuating surface waves at 18 GHz with material parameters $\varepsilon_r = 14.4 - \mathrm{j}0.26$, $\mu_r = 1.44 - \mathrm{j}1.01$ at 18 GHz. The complete frequency behavior of this absorber can be found in [12] and the material library of CST Microwave Studio. The weak-coupling relation in (1) is satisfied and the effects on the mutual coupling are therefore evaluated by simulating the transmission coefficient S_{21} in CST Microwave Studio with an absorber on the left- and right-hand side respectively. It is seen in Fig. 9(b) that placing the absorber on the right-hand side decrease the coupling, and that placing the absorber on the left-hand side increase the coupling at 18 GHz, as predicted by the weak-coupling density, δ in Fig. 8(a). Thus, similar to the previous case in Section III-A, we see that the weak-coupling density can be used to locate regions which contribute to high coupling. In the present case, we note that the streamlines, using (7) could only partly predict regions of strong coupling.

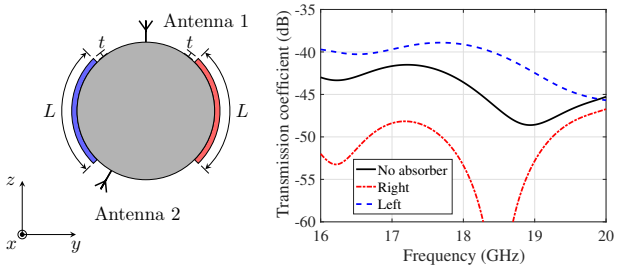

(a) (b)

Fig. 9. (a) Absorbers with $L = \lambda$, $t = 1\,\text{mm}$, and width $w = 0.5\lambda$ along x. (b) S_{21} when the absorbers from (a) is added on one side at the time on the cylinder.

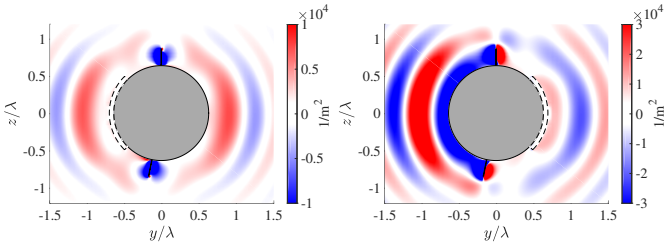

(a) (b)

Fig. 10. Visualization of δ in the yz-plane that contains both the antennas, at 18 GHz when the absorber is added on the (a) left-hand side. (b) right-hand side.

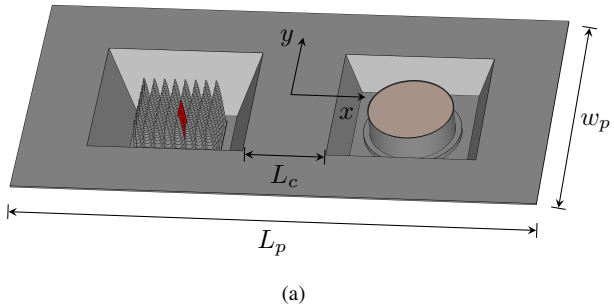

(a)

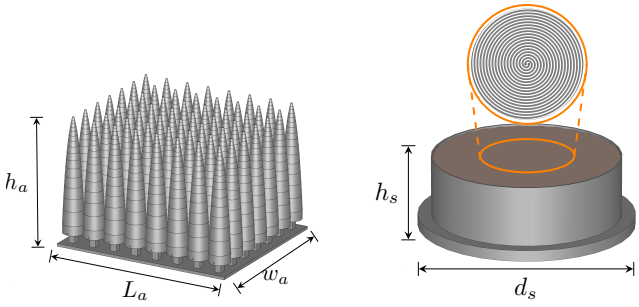

(b) (c)

Fig. 11. (a) Section of a platform with two integrated antennas. Platform dimensions is $L_p = 310\,\text{mm}$, $w_p = 160\,\text{mm}$, and the distance between the cavities is $L_c = 49\,\text{mm}$. (b) BOR-array antenna with 6x8 elements and $L_a = 50\,\text{mm}$, $w_a = 43\,\text{mm}$, and $h_a = 35\,\text{mm}$. (c) Cavity-backed spiral antenna with diameter $d_s = 52\,\text{mm}$ and $h_s = 19.2\,\text{mm}$.

In Fig. 10(a), δ is visualized with an absorber placed on the left-hand side, as highlighted with the black dashed line. It is seen that the region close to the surface on the left-hand side of the cylinder has turned from a negative weak-coupling density region depicted as blue in Fig. 8(a), to a positive weak-coupling density region as depicted with red and white. The contribution from this area is now positive, leading to an increased mutual coupling. Fig. 10(b) illustrates δ when the absorber is placed on the right-hand side and it is seen that the large red area close to the surface on the right-hand side in Fig. 8(a) is reduced, resulting in a decreased coupling.

It has been demonstrated that the weak-coupling density δ is a useful tool when predicting absorber positions that reduce the mutual coupling as well as increase the coupling. Visualizing δ is useful also for larger perturbations of the platform here with larger absorbers. We conclude that the visualization method for the weak-coupling density, which is related to the mutual impedance can be used to obtain accurate information for reducing the mutual coupling, contrary to what is claimed in [11].

C. Integrated Antennas

The third case is a more complex configuration consisting of a ground plane with two cavities for integrating antennas in as seen in Fig. 11. The length and width of the platform is $L_p = 310\,\text{mm}$ and $w_p = 160\,\text{mm}$ with a separation distance $L_c = 49\,\text{mm}$ between the cavities. The configuration could represent a section of an integrated mast of a naval ship, as well as a wingtip on an airplane. The possibilities of using the weak-coupling density to predict where to place absorbers to reduce the mutual coupling between two wideband antennas integrated in a platform is here investigated. A 6x8 element body-of-revolution (BoR) array antenna [25], [26] with length $L_a = 50\,\text{mm}$, width $w_a = 43\,\text{mm}$, and height $h_a = 35\,\text{mm}$ that is depicted in Fig. 11(b) is used and referred to as Antenna 1. The other antenna is a cavity-backed spiral antenna that is shown in Fig. 11(c) and is referred to as Antenna 2. The spiral antenna has a diameter $d_s = 52\,\text{mm}$ and height $h_s = 19.2\,\text{mm}$. The center of the spiral is depicted in the orange inset in Fig. 11(b), and it is designed to intrinsically generates left-hand circular polarization. Both antennas are placed in the respective cavity seen in Fig. 11(a) with the top of the antennas located 1.2 mm below the surface of the platform.

The mutual coupling between a center element in the array, which is highlighted red in Fig. 11(a) and the spiral antenna is studied while the other array elements are terminated with a matched load. Potential absorber locations in this case have been restricted to the flat section of the platform between the two cavities with length $L_c = 49\,\text{mm}$. The considered frequency range is 10–14 GHz. The condition in (1) is satisfied within this band and for the described configuration.

The initial mutual coupling between the antennas depicted in Fig. 11 is shown in Fig. 12(a) as the black dashed curve. It is seen from Fig. 12(a) that the coupling is high around 10.5 GHz, 11.25 GHz, and 14 GHz. The weak-coupling density δ is therefore visualized in the xy-plane for $z = 1\,\text{mm}$ above the platform at these frequencies with (5), using $\hat{\boldsymbol{n}} = -\hat{\boldsymbol{x}}$. Fig. 13 depicts the result, where the black dashed lines high-

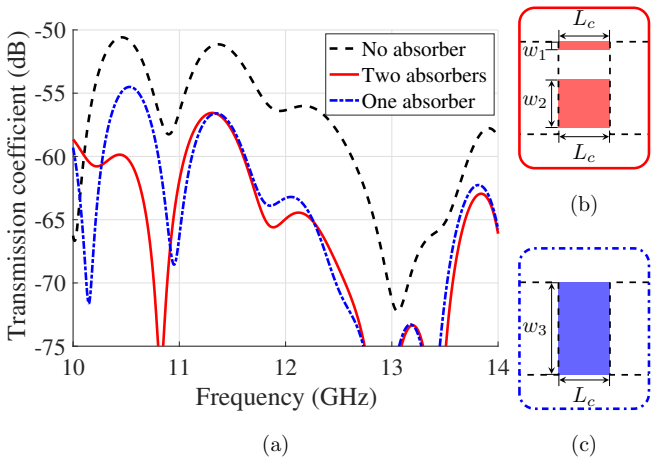

Fig. 12. (a) Mutual coupling between the array element and the spiral without absorbers (black dashed), with two absorbers according to Fig. 12(b) (red solid), with one absorber according to Fig. 12(c) (blue dash-dotted). (b) Absorbers placed based on δ. (c) An absorber covering the surface between the cavities.

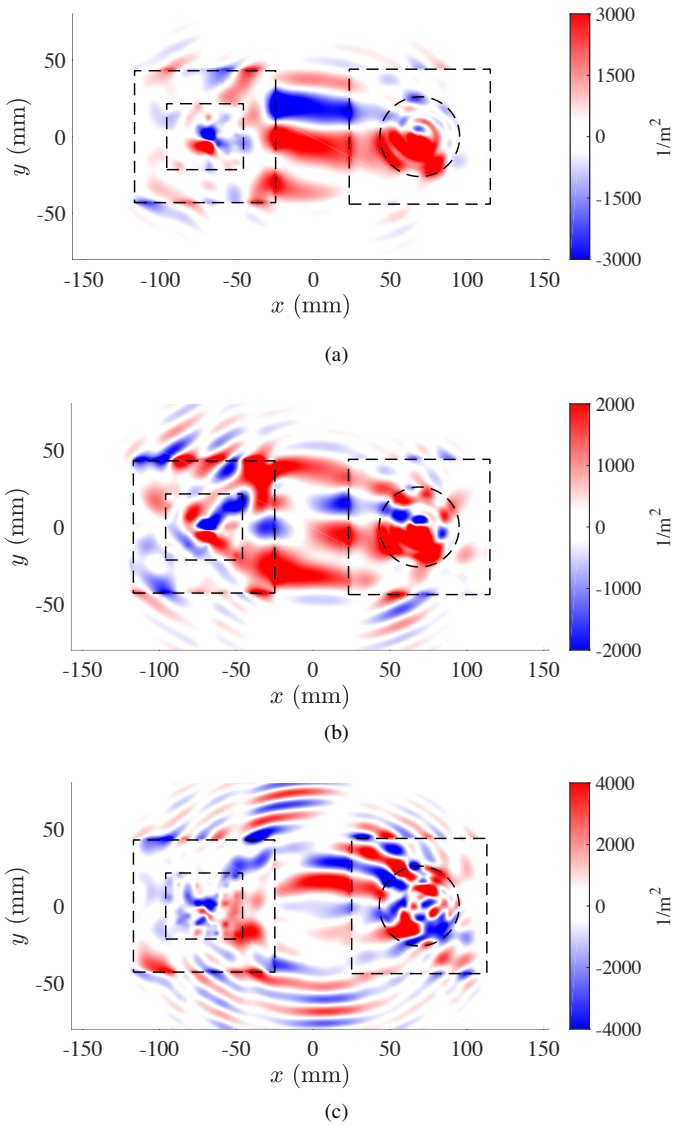

Fig. 13. Visualization of δ in the xy-plane for $z = 1$ mm above the platform at: (a) 10.5 GHz. (b) 11.25 GHz. (c) 14 GHz.

lights the location of the cavities and the antennas. A dominant red region is seen at 10.5 GHz and 11.25 GHz that ranges from $y = 0$ mm to $y \approx -44$ mm between the cavities. At 14 GHz this region is dominantly red corresponding to positive weak-coupling density, although it contain some smaller blue regions corresponding to a negative weak-coupling density. The region between $y = 0$ mm to $y \approx 15$ mm is red at 14 GHz. Furthermore, a narrow red region is seen between the two cavities around $y = 40$ mm at 10.5 GHz, 11.25 GHz, and partially at 14 GHz.

Based on the visualization results in Fig. 13, absorbers are placed on the surface between the two cavities, according to Fig. 12(b). The upper absorber has a width $w_1 = 8$ mm and is centered at $x = 0$ mm, $y = 40$ mm. The lower absorber has a width $w_2 = 46$ mm, and is centered at $x = 0$ mm, $y = -15$ mm. Both absorbers has a thickness of 1 mm and length $L_c = 49$ mm. The type of absorber used is the same SWAM [24] as used in Section III-B. The red solid curve in Fig. 12(a) represents a simulation of the transmission coefficient with the absorbers placed according to Fig. 12(b). It is seen that the mutual coupling is reduced from 10.2-14 GHz when the absorbers are placed based on the visualization of the weak-coupling density in Fig. 13.

The naive solution of covering the whole surface between the two cavities with an absorber is also investigated. An absorber with length $L_c = 49$ mm, width $w_3 = 88$ mm, and thickness 1 mm that is centered in origin is placed between the cavities as shown in Fig. 12(c). The blue dash-dotted curve in Fig. 12(a) is the simulated mutual coupling with the absorber Fig. 12(c) present. It is seen that the mutual coupling is 5 dB higher at 10.5 GHz when the whole surface is covered by an absorber, compared to placing absorbers according to Fig. 12(b), which is based on the weak-coupling density. Covering the whole surface between the cavities with an absorber reduces the negative weak-coupling density region as depicted in blue centered at $y = 20$ mm in Fig. 13(a), which explain why the mutual coupling is higher, compared to placing absorbers based on the weak-coupling density. From Fig. 13(b) and Fig. 13(c) it is seen that placing an absorber on the whole surface, compared to placing absorbers according to Fig. 12(b) will reduce both red and blue regions. This describes why the difference between the the two absorber configurations are small in terms of mutual coupling at 11.25 GHz and 14 GHz.

The weak-coupling density has been used to systematically reduce the mutual coupling between two wideband antennas placed on a common platform with satisfying result. By visualizing the weak-coupling density δ at several frequencies it is possible to predict absorber positions that will reduce the mutual coupling over a band of frequencies.

IV. Conclusion

In this paper, a visualization method for identifying regions around a platform with strong contributions to the mutual

coupling is proposed. The presented real-valued time-invariant quantity is named the weak-coupling density.

The weak-coupling density has here been tested in numerical simulations to predict absorber positions in three different cases to systematically reduce the mutual coupling between two antennas with good results. The correlation between a large weak-coupling density and a large impact on the mutual coupling is high. This predictability is robust to the shape of the platform and it persists over neighboring frequency bands. It is furthermore easy to determine.

The weak-coupling density has been compared with the Poynting vector based method. The here presented method predicts good absorber locations. Indeed, placing a small absorber at the strongest predicted weak-coupling density position gave a larger reduction of the mutual coupling than when the same absorber were placed at the position predicted by the Poynting vector based method, in the investigated cases.

The weak-coupling density also has the feature in its visualization that it can predict several different locations to place absorbers and it also indicates regions where absorber placement would increase the mutual coupling. As a comparison the Poynting vector based method in the tested implementations tends to show a coupling path with less predicative information regarding a reduction of the coupling. Furthermore, it is clearly demonstrated that it is possible to achieve a lower mutual coupling with less absorber material when placing them based on visualizing the weak-coupling density, as compared to covering the whole available space.

The ability to distinguish between regions where the placement of absorbers would reduce or increase the mutual coupling, together with the straightforward interpretation of the results, makes the weak-coupling density a useful method for systematically reducing mutual coupling. A nice feature of the proposed method is that it is easy to implement the calculation of the weak-coupling density as a post-processing step in full-wave electromagnetic software.

REFERENCES

[1] T. M. Macnamara, *Introduction to antenna placement and installation*, Chichester, UK: John Wiley & Sons, 2010.

[2] E. F. W. Alexanderson, "Simultaneous sending and receiving," *Proc. IRE*, vol. 7, no. 4, pp. 363–378, 1919.

[3] Z. Li, Z. Du, M. Takahashi, K. Saito, and K. Ito, "Reducing mutual coupling of MIMO antennas with parasitic elements for mobile terminals," *IEEE Trans. Antennas Propag.*, vol. 60, no. 2, pp. 473–481, 2012.

[4] S. Zhang, Z. Ying, J. Xiong, and S. He, "Ultrawideband MIMO/diversity antennas with a tree-like structure to enhance wideband isolation," *IEEE Antennas Wireless Propag. Lett.*, vol. 8, pp. 1279–1282, 2009.

[5] E. Rajo-Iglesias, O. Quevedo-Teruel, and L. Inclan-Sanchez, "Mutual coupling reduction in patch antenna arrays by using a planar EBG structure and a multilayer dielectric substrate," *IEEE Trans. Antennas Propag.*, vol. 56, no. 6, pp. 1648–1655, 2008.

[6] J. Zhang, S. Yan, X. Hu, and G. A. Vandenbosch, "Mutual coupling suppression for on-body multiantenna systems," *IEEE Trans. Electromagn. Compat.*, vol. 62, no. 4, pp. 1045–1054, 2020.

[7] H. H. Park, "Reduction of electromagnetic noise coupling to antennas in metal-framed smartphones using ferrite sheets and multi-via EBG structures," *IEEE Trans. Electromagn. Compat.*, vol. 60, no. 2, pp. 394–401, 2018.

[8] D. Sievenpiper, L. Zhang, R. F. Broas, N. G. Alexopolous, and E. Yablonovitch, "High-impedance electromagnetic surfaces with a forbidden frequency band," *IEEE Trans. Microw. Theory Techn.*, vol. 47, no. 11, pp. 2059–2074, 1999.

[9] H. Frid, "Analysis and optimization of installed antenna performance," Ph.D. dissertation, KTH Royal Institute of Technology, 2020.

[10] J. Malmström, H. Holter, and B. L. G. Jonsson, "On mutual coupling and coupling paths between antennas using the reaction theorem," *IEEE Trans. Electromagn. Compat.*, vol. 60, no. 6, pp. 2037–2040, 2018.

[11] Y. Zhong, W. Song, C. Kim, and C. Hwang, "Coupling path visualization and its application in preventing electromagnetic interference," *IEEE Trans. Electromagn. Compat.*, vol. 62, no. 4, pp. 1485–1492, 2020.

[12] J. Lundgren, "Visualizing and controlling coupling paths between antennas installed on common platforms," M.S. thesis, Division Electromagn. Eng., KTH Royal Institute of Technology, Stockholm, Sweden, Jun. 2020.

[13] V. H. Rumsey, "Reaction concept in electromagnetic theory," *Phys. Rev.*, vol. 94, no. 6, pp. 1483–1491, 1954.

[14] J. H. Richmond, "A reaction theorem and its application to antenna impedance calculations," *IRE Trans. Antennas Propag.*, vol. 9, no. 6, pp. 515–520, 1961.

[15] T. Kurner, D. J. Cichon, and W. Wiesbeck, "Concepts and results for 3D digital terrain-based wave propagation models: An overview," *IEEE J. Sel. Areas Commun.*, vol. 11, no. 7, pp. 1002–1012, 1993.

[16] V. Degli-Esposti, D. Guiducci, A. de'Marsi, P. Azzi, and F. Fuschini, "An advanced field prediction model including diffuse scattering," *IEEE Trans. Antennas Propag.*, vol. 52, no. 7, pp. 1717–1728, 2004.

[17] H. Li, V. V. Khilkevich, and D. Pommerenke, "Identification and visualization of coupling paths—part I: Energy parcel and its trajectory," *IEEE Trans. Electromagn. Compat.*, vol. 56, no. 3, pp. 622–629, 2014.

[18] H. Li, V. V. Khilkevich, and D. Pommerenke, "Identification and visualization of coupling paths—part II: Practical application," *IEEE Trans. Electromagn. Compat.*, vol. 56, no. 3, pp. 630–637, 2014.

[19] A. Talebzadeh, P. C. Sochoux, J. Li, Q. Liu, K. Ghosh, and D. Pommerenke, "Shielding effectiveness, coupling path, and EMI mitigation for QSFP cages with heatsink," *IEEE Trans. Electromagn. Compat.*, vol. 60, no. 5, pp. 1254–1262, 2018.

[20] A. Talebzadeh, P. K. Vuppunutala, K. Koo, H. Li, J. Nadolny, Q. Liu, J. Li, K. Ghosh, P. C. Sochoux, V. Khilkevich *et al.*, "Coupling path visualization and EMI mitigation for flyover QSFP connectors," *IEEE Trans. Electromagn. Compat.*, vol. 62, no. 4, pp. 1037–1044, 2020.

[21] H. Li, V. Khilkevich, D. Pommerenke, Y. Zhang, and J. Fan, "On the possibility to detect and visualize electromagnetic coupling paths," in *Proc. IEEE Int. Symp. Electromagn. Compat.*, Aug. 2011, pp. 559–563.

[22] R. E. Collin, *Foundations for microwave engineering*, New York, NY, USA: John Wiley & Sons, 2007.

[23] J. Malmström, "Derivation of reaction theorems for scattered fields," *IEEE Antennas Wireless Propag. Lett.*, vol. 17, no. 10, pp. 1876–1880, 2018.

[24] *"Microwave Absorbing Materials"* Laird Technologies. Accessed on: Nov. 4, 2020. [Online]. Available: https://www.mouser.com/pdfdocs/LairdEMIAbsorbers-2.pdf.

[25] H. Holter, "Dual-polarized broadband array antenna with BOR-elements, mechanical design and measurements," *IEEE Trans. Antennas Propag.*, vol. 55, no. 2, pp. 305–312, 2007.

[26] H. Frid, J. Malmström, and B. L. G. Jonsson, "Determining direction-of-arrival accuracy for installed antennas by postprocessing of far-field data," *Radio Sci.*, vol. 54, no. 12, pp. 1204–1221, 2019.